Imaging Divertor Strike Point Splitting in RMP ELM Suppression Experiments[a)]

R. A. Moyer,[1,b)] I. Bykov,[1] D.M. Orlov,[1] T.E. Evans,[2] J.S. Lee,[3], A.M. Teklu,[4] M.E. Fenstermacher,[5], M. Makowski,[5], C.J. Lasnier,[5], H.Q. Wang,[6], J.G. Watkins,[7] and W. Wu[2]

[1]*Center for Energy Research, University of California San Diego, La Jolla, California 92093-0417, USA*
[2]*General Atomics, San Diego, California 92186-5608, USA*
[3]*University of California Los Angeles, Los Angeles California 90095, USA*
[4]*Oregon State University, Corvallis, Oregon 97331, USA*
[5]*Lawrence Livermore National Laboratory, Livermore, California 94550, USA*
[6]*Oak Ridge Associated Universities, Oak Ridge, Tennessee 37831, USA*
[7]*Sandia National Laboratories, California, Livermore, California 94551-0969, USA*

(Presented XXXXX; received XXXXX; accepted XXXXX; published online XXXXX)
(Dates appearing here are provided by the Editorial Office)

Fast visible imaging of the lower divertor is used to study the structure and dynamics of lobes induced by resonant magnetic perturbations (RMPs) in ELM suppression experiments in DIII-D. The best compromise between amount of light and sharp imaging was obtained using emission at 601 nm from Fulcher band molecular deuterium emission. Multiple spatially resolved peaks in the D_2 emission, taken as a proxy for the particle flux, are readily resolved during RMPs, in contrast to the heat flux measured by infrared cameras, which shows little spatial structure in ITER-like conditions. The 25 mm field lens provides high spatial resolution (2–4 mm/pixel) from the centerpost to the outer shelf over 40° toroidally that overlaps the field of view of the IRTV that measures the divertor heat flux, allowing direct comparison in non-axisymmetric discharges. The image is coupled to a Phantom 7.3 camera using a Schott wound fiber bundle, providing high temporal resolution that allows the lobe dynamics to be resolved between ELMs and across ELM suppression onset. These measurements are used to study the heat and particle flux in 3D magnetic fields, and to validate models for the plasma response to RMPs.

I. MOTIVATION FOR DIVERTOR STRIKE POINT IMAGING

The structure of divertor heat and particle fluxes are critical issues for ITER and other next-step burning tokamaks[1]. Concerns range from prediction of a radially narrow inter-ELM heat flux[2] to impact of divertor strike point splitting by magnetic field perturbations from locked modes[3,4] and ELM suppression coils[5–7] on particle and heat fluxes, which is problematic for tightly baffled divertors. In addition, the evolution of the wall fuel and impurity source through an ELM cycle is important for understanding the role of different fueling channels in H-mode pedestal recovery, trapping of impurities in the divertor, and providing boundary conditions for integrated core-edge modeling[8]. Fast visible imaging of the photon fluxes from the divertor strike points can be used to constrain modeling of boundary fueling and transport, and to validate equilibrium reconstructions (strike point location) and simulations of plasma response to the RMPs used to suppress ELMs in tokamak H-modes[9–12].

Imaging of emission lines in the visible to near-infrared range (400-1000nm) provides significant advantages for studying transient events requiring either fast temporal response (ELMs), high spatial resolution (arcing or dust), or large toroidal extent (strike point asymmetry). Imaging in DIII-D provides continuous data with high spatial resolution (2–4 mm/pixel) that spans the radial extent of the divertor over a 40° toroidal range, unlike divertor Langmuir probes and Thomson scattering which have limited spatial and/or temporal resolution.

The requirements for effective fast visible imaging of photon fluxes from emission lines in the divertor include high transmission of the optical system and quantum efficiency of the camera in the relevant wavelength range; protection from stray magnetic fields; resistance to γ-ray, hard X-ray, and neutron radiation; the possibility of absolute photon flux calibration; sufficient photon flux to allow high framing rates to study transient events (ELMs, detachment onset, etc.); and a sufficiently wide angle of view to study radial profiles and toroidal asymmetries. Cameras can be used to meet these requirements in either single-color or multi-color mode.

II. DESIGN OF THE DIII-D FAST VISIBLE IMAGING SYSTEM (FASTCAM)

Three Vision Research Phantom cameras are used for these measurements at DIII-D[13]. Each camera has a CMOS detector with 22μm pixels that yield 2–4mm spatial

[a)]Published as part of the Proceedings of the 22nd Topical Conference on High-Temperature Plasma Diagnostics (HTPD 2018) in San Diego, California, USA.
[b)]Author to whom correspondence should be addressed: moyer@fusion.gat.com.

resolution in the divertor, and a maximum resolution of 800x600 pixels in the (ϕ,R) plane. These cameras have a resolution-dependent exposure time with a minimum of 1 μs. One camera is a Phantom v7.1, with 12 bit image depth and 2.8Gbytes RAM; the other two cameras are Phantom v7.3s, with 14 bit image depth and 10 and 32Gbytes RAM respectively.

The CMOS cameras are sensitive to both magnetic fields and ionizing radiation, so the camera is installed in an enclosure remote (2–3m) from the vessel that shields magnetic fields, neutrons, and γ-rays (FIG. 1). The magnetic shield consists of 0.375 inch thick low carbon steel, which reduces |B|~210G at the camera location to ~15G. The radiation shield is wrapped around the magnetic shield, and consists of a 3 inch thick outer layer of green borated polyethylene (neutron moderation and capture) with an inner layer of 0.25 inch thick lead for shielding γ-rays produced by neutron absorption in the machine hall and inside the neutron shield.

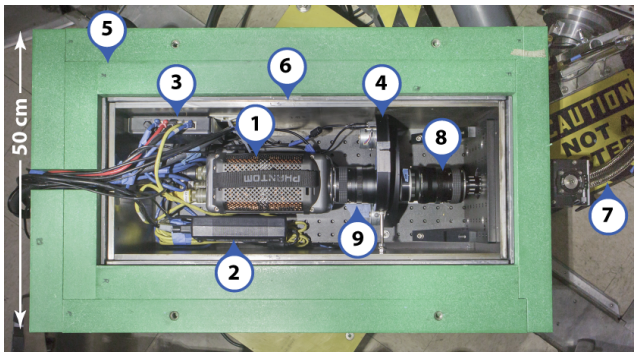

FIG. 1. DIII-D fast camera and shield box enclosure: (1) Phantom CMOS camera; (2) camera power supply; (3) communications link; (4) duel 2 inch filter wheels; (5) neutron shielding; (6) γ-ray and magnetic shielding; (7) coherent fiber bundle; (8) and (9) relay optics.

A Schott IG-163 silicate glass wound fiber bundle[14], is used to transfer the image from a Schneider 25mm field lens on the 75° R+2 port of the tokamak [FIG. 2(a)] to the camera inside the shield box. Matched 50mm relay lens are used to couple the filter wheels to the end of the fiber, and to parallelize the rays to minimize shifts in the interference filter band pass across the FOV. The fiber bundle allows the camera to be used for a variety of measurements on several ports within reach of the fiber bundle (9 or 14 feet long), including primarily a tangential view in the co-plasma current I_p direction at toroidal angle ϕ = 90° [FIG.2(b)]. A significant drawback of the fiber bundle is the degradation of transmission due to exposure to hard X- and γ-rays and to neutrons in the machine hall. This darkening of the fibers can be annealed with high temperature baking of the fiber bundles (180–200°C) for about 20–25 cycles[15].

The divertor shelf (1.85≤S≤2.24) obscures the view of the outer strike point for plasmas with the strike point positioned for pumping, as indicated by the discontinuity in the red line in FIG. 2(a). However, the outer divertor can be imaged when the strike point is moved inward from the shelf or placed on the shelf. An important aspect of the

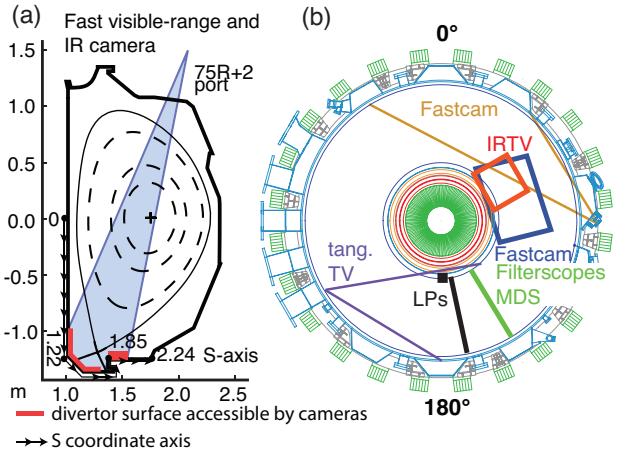

FIG. 2. (a) DIII-D poloidal cross-section showing the 25mm field lens for FASTCAM divertor imaging on the 75° R+2 port. The blue shaded region is the field of view (FOV) through the plasma to the lower divertor surfaces (red line) accessible to the camera. The black line with arrowheads is the S-coordinate axis used to map the divertor data to physical space, with representative values indicated in meters. (b) Toroidal cross-section showing the location of the divertor diagnostics used in this imaging, including: (brown) 90° tangential FASTCAM FOV; (red box) IRTV FOV; (blue box) 75° FASTCAM FOV; (green line) radius of filterscope and Multi-chord Divertor Spectrometer views; (black) floor Langmuir probes; and (purple) FOV of the lower divertor tangential TV.

camera divertor view [FIG. 2(b)] is the overlap with the infrared TV (IRTV) view at ϕ = 60° used to measure the heat flux to the divertor. This allows the radial profiles of the particle and heat flux to be compared for the first time at the same ϕ, an important capability for studying non-axisymmetric discharges such as those used for RMP ELM suppression.

III. EMISSION LINES USED IN FAST DIVERTOR IMAGING

For fast imaging of transients in the divertor, the FASTCAM system is used in one-color mode with narrow-band interference filters to selection emission lines of interest in the visible range. Two common examples for inferring D^+ ion flux are shown in FIG. 3: (a) molecular D_2 emission from the rotational-vibrational Fulcher band around 601 nm, overlaid in orange on the divertor view for reference, and (b) neutral atomic Balmer-α emission (656.3 nm). For the image resolution shown (512x368 pixels), the maximum framing rate is ~15kfps. Under typical conditions, the Balmer-α emission allows exposure times as low as 3 μs; by reducing the image resolution (FOV), it is possible to frame as fast as 200kfps. The remaining lines of interest are more than an order of magnitude dimmer. Typical framing rates and exposure times are: 5kfps and 198 μs for D_2; and 2–5 kfps and 498–198μs for CII and CIII. These framing rates are fast enough to resolve inter-ELM dynamics. The FASTCAM system can also be operated in four-color mode, using a Photometrics QV2 beam splitter[16] when simultaneous

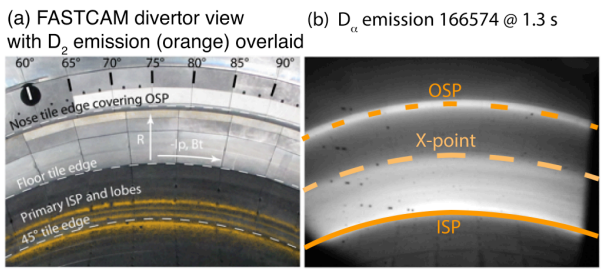

FIG. 3. (a) Image of the lower divertor chanber with the D_2 Fulcher-α emission from RMP ELM suppression discharge 166450 at 2.8 s overlaid in orange. Four distinct bands of emission are clearly visible at the inner strike point (bottom of image). (b) Image of the lower divertor in neutral deuterium Balmer-α emission for a detached divertor discharge, resulting in a broad band of emission extending from the inner strike point (solid line) up the divertor leg to the divertor X-point (large dashed line). The outer strike point (OSP) is visible just inboard of the nose time (short dashed line).

imaging of multiple lines is required[8], although the beam splitter significantly reduces the framing rate.

In FIG. 3(a), the outer strike point (OSP) is placed in the entrance to the pumping plenum under the shelf (FIG. 2) to reduce the discharge density and collisionality via active pumping. As shown in Fig. 2, the OSP is consequently not visible due to the nose tile of the shelf. The inner strike point (ISP), however, is readily visible and shows 4 well resolved peaks in the D_2 photon flux due to the perturbation of the ISP by the n = 3 applied RMP. In the discharge in Fig. 3(b), the OSP has been pulled to smaller major radius by 2.2 cm, allowing the primary OSP (short dashed line) to be seen. At the ISP (solid line), in place of the emission structures at the divertor surface in (a), the emission extends above the divertor floor along the inner leg of the divertor up to the X-point (large dashed line) and up the plasma edge due to detachment of the plasma at the ISP. These results indicate that fast visible imaging of the molecular D_2 Fulcher band can be used to measure the splitting of the ISP provided that the ISP remains attached, as it does during the ITER-like low collisionality and density conditions typical of RMP ELM suppression experiments in DIII-D[11,17].

IV. D_2 PHOTON FLUX AS PROXY FOR D^+ ION FLUX

Photon fluxes are obtained from camera images (FIG. 3) by applying an absolute brightness calibration that accounts for the wavelength-dependent transmission of the vessel port, fiber bundle, and interference filter, as well as the camera exposure time and detector response. In ionizing plasmas, there is a balance between the flux of neutral or low charge state fuel and impurity particles from the wall Γ and ionization sink Γ_i to higher charge states. Thus, the measured photon flux Φ from lower charge state impurities and neutral fuel can be used for calculating the corresponding wall source using the inverse photon efficiency (number of ionization events per photon) S/XB, the ratio of the electron ionization S to excitation X rate coefficients and the branching ratio B. S/XB is a function of local n_e and T_e at the strike point: $S/XB(n_e,T_e)=\Gamma(n_e,T_e)/\Phi(n_e,T_e)$, where divertor Langmuir probes or Thomson scattering are used to measure n_e and T_e. Applying this method to atomic Balmer-α photon fluxes Φ_D is complicated by contributions to D re-emission from the wall from chemical erosion products C_xD_y, and because D is released from the wall in both atomic D and molecular D_2 forms. Consequently, despite the simplicity of the spectroscopic measurement of atomic Balmer-α emission, the total D source must be inferred by using an effective factor $(S/XB)_{eff}$, such that $\Gamma^D_{tot} = (S/XB)_{eff} \times \Phi_{D_\alpha}$. Bykov *et al.* have measured $(S/XB)_{eff} \approx 2 \times S/XB \approx 40$ for attached divertor plasmas in L and ELMing H-modes in DIII-D[8]. A similar result was obtained in TEXTOR[9].

The D atom flux re-emitted as molecules Γ^D_{mol} can be similarly determined from the total Fulcher band photon flux Φ_{Ful} as $\Gamma^D_{mol} = 2D/XB \times \Phi_{Ful}$, where *D/XB* is the photon efficiency for molecular dissociation, and Φ_{Ful} is the total Fulcher band intensity, which consists of multiple rotational-vibrational lines spanning the range from 600-640 nm. It is not practical to measure the entire Fulcher band intensity with a wide band pass filter because of multiple contaminant lines in that wavelength range. To avoid this problem, we use a filter to measure the intensity of the first diagonal band (around 601 nm), as shown in FIG. 4. The intensity of this first diagonal band (transitions with equal vibrational number v=v'=0) can be extrapolated to that of the full Fulcher band Φ_{Ful} using a collisional radiative model (CRM)[18]. The molecular photon flux is a good proxy for the particle flux from the target because in attached divertor conditions in L and ELMing H-mode plasmas, the molecules are formed at the surface and account for 80–90% of the total recycling D[6]. An advantage of imaging the molecular rather than the atomic photon flux is locality of the emission because D_2 molecules are slow compared to D and quickly dissociate within a mean free path of a few mm. Given that the recycling fraction is nearly 1, this provides an accurate footprint of the incident ion flux $\Gamma_{D^+}$and is preferred over imaging of the Gerö band (~430 nm) of chemically eroded CD molecules.

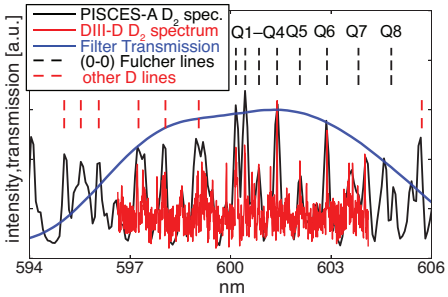

FIG. 4. D_2 Fulcher band spectra from: (black solid line) the PISCES-A linear plasma device using a fast, low resolution Avantes D_2 spectrometer, and (red solid line) DIII-D using the Multi-chord Divertor Spectrometer (MDS). The solid blue line is the D_2 filter transmission, which passes the first 8 diagonal components of the Q(0-0) band, marked by the black dashed lines, as well as other D lines indicated by the dashed red lines[9].

V. DIVERTOR STRIKE POINT SPLITTING IN RMP ELM SUPPRESSION DISCHARGES

Edge resonant magnetic field perturbations (RMPs) are used in DIII-D to control the impulsive power loading to the divertor targets due to edge localized modes (ELMs). In ITER, ELMs are predicted to release 20-30 MJ of plasma stored energy on very short timescales (<1 ms), producing significant erosion and damage to the targets, and reducing the divertor lifetime to as little as a single large ELM[1,19]. In 2003, Evans and Moyer demonstrated that ELMs could be suppressed by application of 1 part in 10000 magnetic field perturbations that were resonant near the top of the H-mode pedestal[11]. These magnetic fields perturb the separatrix which forms the topological boundary between closed and open magnetic field lines in a diverted plasma. The non-axisymmetric perturbation lifts the degeneracy of the stable and unstable manifolds [Fig. 5(a)] which define the axisymmetric separatrix, forming lobes which narrow in width and increase in amplitude (magnetic flux-preserving) as the divertor X-point is approached [Fig. 5(a)]. When these lobes are long enough, they intersect the divertor target, causing the axisymmetric strike point to split into multiple lobes[19–21]. These lobes have been shown to change plasma edge profiles[22,23], and to modulate the particle flux to the divertor[5–7]. However, for reasons that are not yet well understood, there is little effect on the divertor heat flux profile. Because such splitting of the divertor heat flux can present problems in ITER and other tokamaks with tight divertor baffling, there is considerable interest in understanding the impact of the plasma response to the applied RMP on these structures, and the lack of heat flux dependence on these structures. Fast visible imaging of the divertor particle flux in the (R,ϕ) plane of the divertor, in conjunction with infrared imaging of the divertor heat flux within the same toroidal span, provides a powerful tool for studying the impact of this strike point splitting on divertor heat flux, and for validating equilibrium reconstructions and models of the plasma response to the RMPs.

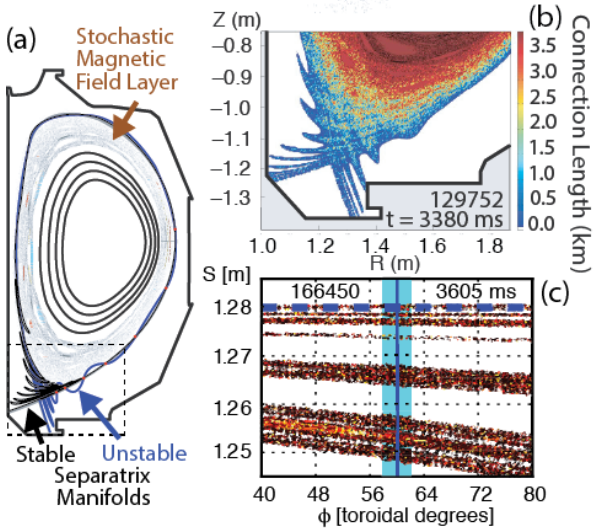

FIG.5. (a) DIII-D poloidal cross-section showing a stochastic magnetic field layer with embedded island remnants in the outer edge due to RMPs. The RMPs deform the separatrix into unstable (blue) and stable (black) manifolds that oscillate with increasing amplitude and narrower width as the X-point is approached. (b) Enlargement of the divertor region, with colors indicating the magnetic field line connection length,. (c) Map of the hit points in (S,ϕ) of magnetic fields lines integrated from inside the separatrix. When the lobes in (b) intersect the divertor target, the axisymmetric strike point (blue dashed line) splits into n bands of field line hits, where n is the toroidal mode number of the applied perturbation, which wrap around the torus twice at this toroidal angle. The solid blue vertical line is the ϕ of the heat flux measurement and the light blue box is the toroidal range for averaging the D_2 photon flux measurement.

An example of the measured splitting of the particle flux in the divertor of RMP ELM suppression discharge 166450 in DIII-D is shown in FIG. 3(a). In FIG. 6, the D_2 photon flux is plotted versus time and S-coordinate in the vicinity of the ISP [Fig. 2(a)] after averaging over $\Delta\phi=4°$ centered on $\phi=60°$ where the divertor heat flux is measured by the IRTV [Fig. 2(b)]. Blue corresponds to the lowest and red to the highest measured photon flux. The ELM behavior is shown by the blue Balmer-α intensity measured by the filterscopes in the middle frame. The RMP is applied at 2.0 s, as shown in the bottom frame. At 2.5 s, the current in one quartet of RMP coils is ramped to change the dominant toroidal mode number n of the RMP from 3 to 2. Shortly after the end of this RMP current ramp, the plasma returns to ELMing H-mode at 3.7 s. The dashed line shows the location of the primary ISP

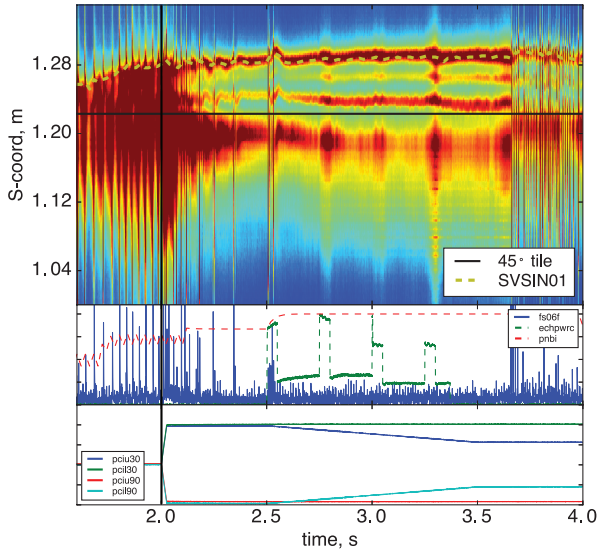

FIG. 6. (top) D_2 photon flux (ph/cm2/s) versus divertor S-coord. and time. The dashed line SVSIN01 indicates the ISP position from EFIT reconstructions constrained by external magnetics only. The horizontal black line is the transition from the centerpost (S < 1.22 m) to the 45° sloped divertor tile (S > 1.22 m). The vertical black line is the onset of the RMP. (middle) Time traces of: (blue) Balmer-α emission near the ISP, showing the ELM behavior; (red) neutral beam injected power; and (green) Electron Cyclotron Heating (ECH) power. (bottom) Time traces of the RMP coil currents in the 30° and 90° upper and lower RMP coil segments, showing the ramp from n = 3 (t < 2.5 s) to n = 2 (t> 3.5 s).

calculated from EFIT equilibrium reconstruction using only the external magnetics data[24]. The ELMs transiently broaden the primary strike point until the RMP is applied, after which the ELMs suppress and 4 discrete peaks in the D_2 photon flux are formed at the ISP. As the RMP current is ramped, the plasma control system holds the primary strike point at constant S, while the remaining three lobes move in radius and the D_2 photon flux intensity changes.

The radial structure of the particle and heat fluxes is

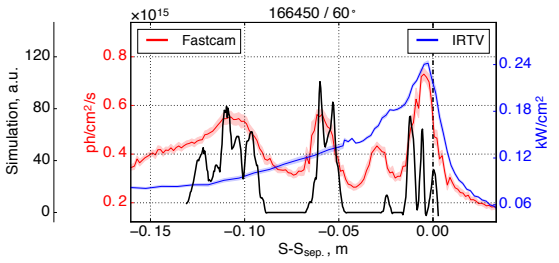

FIG. 7. Radial profiles of (red) the D_2 photon flux, (blue) the heat flux, and (black) the magnetic field line hit point density weighted by the field line connection length at 2.75 s in RMP ELM suppression discharge 166450 at $\phi = 60°$. The heat flux profile has been shifted by ~2cm to align the peak with the D_2 photon flux. The field line hit density $S-S_{sep}$ has been multiplied by 4 for this comparison.

compared in Fig. 7 at 2750 ms. The 4 peaks in the D_2 photon flux are clearly visible. The IRTV heat flux measurement shows only small "shoulders" near the positions of the well resolved peaks in the particle flux. Calculations of the radial profile of the magnetic field line hit density using the vacuum magnetic field line integration code TRIP3D[25] show excellent agreement with the 4 peaks in the D_2 photon flux when the TRIP3D $S-S_{sep}$ is multiplied by 4, which is consistent with previous DIII-D results[22,23,26]. Because linear plasma response modeling with MHD codes indicates that the plasma response is dominantly a screening response[12], which has been shown to *reduce* the strike point splitting *below* the vacuum model predictions[23], the measured particle flux splitting presents a challenge for existing plasma response models. Such time-dependent measurements of the particle flux splitting during RMP experiments can be used to validate the plasma response models.

VI. SUMMARY

Fast visible imaging of the divertor provides time-dependent, spatially resolved measurements of D and C particle fluxes in attached plasma conditions in DIII-D. These fluxes can be used to study the fueling and recovery of the H-mode pedestal in the inter-ELM period[8], to verify equilibrium reconstructions with the strike point positions, and to validate simulations of the plasma response to magnetic field perturbations used to suppress ELMs.

VII. ACKNOWLEDGEMENTS

This material is based upon work supported by the U.S. Department of Energy, Office of Science, Office of Fusion Energy Sciences, under Award Numbers DE-FG02-07ER54917, DE-FG02-05ER54809, DE-FC02-04ER54698, DE-AC52-07NA27344, DE-NA0003525, and DE-AC04-94AL85000. This research used resources of the DIII-D National Fusion Facility, which is a DOE Office of Science User Facility.

VIII. DISCLAIMER

IX. REFERENCES

[1]A. Loarte *et al.*, Nuclear Fusion **54** 033007 (2014).
[2]R.J. Goldston, Nucl. Fusion **52** 013009 (2012).
[3]T.E. Evans *et al,* J. Nucl. Mater. **220-222**, 235 (1995).
[4]C.J. Lasnier *et al.,* Nucl. Fusion **38**, 1225 (1998).
[5]M. Jakubowski, *et al.,* Nucl. Fusion **49** 095013 (2009).
[6]O. Schmitz *et al.,* Plasma Phys. Control. Fusion **50** 124029 (2008).
[7]A. Wingen, O. Schmitz, T.E. Evans, and K.H. Spatschek, Phys. Plasmas **21** 012509 (2014).
[8]I. Bykov, *et al.,* "ELM-resolved characterization of the fuel and impurity source in the divertor of DIII-D," submitted to: Nucl. Fusion (2018).
[9]Ph. Mertens and S. Brezinsek, Fusion Sci. Technol. **47** (2005) 161.
[10]T.E. Evans, *et al.,* Phys. Rev. Lett. **92** 235003-1 (2004).
[11]T.E. Evans, *et al.,* Nature Physics **2** 419 (2006).
[12]R.A. Moyer, *et al.,* Phys. Plasmas **24** 102501 (2017).
[13]Vision Research Phantom v7.3, www.phantomhighspeed.com/products/phantom-high-speed-cameras-super-slow-motion-cameras/v73.
[14]Schott North America Inc., 2014 Wound Fiber Optic Image Bundles, (www.us.schott.com/lightingimaging/english/products/machinevision/fiberoptics/wound.html).
[15]C.P. Chrobak, M.A. Van Zeeland, R.A. Moyer, and J.H. Yu, Rev. Sci. Instrum. **83** 10E514, (2012).
[16]Photometrics QV2 Multichannel Imaging System, www.photometrics.com/products/multichannel/qv2.php.
[17]K.H. Burrell, *et al.,* Plasma Phys. Control. Fusion **44** A253 (2002).
[18]S. Brezinsek, *et al.,* J. Nucl. Mater. 313316 967 (2003).
[19]G. Federici, *et al.,* J. Nucl. Mater. **313–316** 11 (2003).
[19]T.E. Evans, R.K.W. Roeder, J.A. Carter, B.I. Rapoport, M.E. Fenstermacher, and C.J. Lasnier, J. Phys. Conf. Ser. **7** 174 (2005).
[20]T.E. Evans, R.K.W. Roeder, J.A. Carter, and B.I. Rapoport, Contrib. Plasmas Phys. **44** 235 (2004).
[21]R.K.W. Roeder, B.I. Rapoport, and T.E. Evans, Phys. Plasmas **10** 3796 (2003)
[22]R.A. Moyer, *et al.,* Nucl. Fusion **52** 123019 (2012).
[23]D.M. Orlov, *et al.,* Nucl. Fusion **54** 093008 (2014).
[24]L.L. Lao, H. St. John, R.D. Stambaugh, A.G. Kellman, and W. Pfeiffer, Nucl. Fusion **25** 1611 (1985).
[25]T.E. Evans, R.A. Moyer, and P. Monat, Phys. Plasmas **9** 4957 (2002).
[26]T. E. Evans, I. Joseph, R. A. Moyer, et al., J. Nucl. Mater. **363-365** 570 (2007).